Nonlinear operation of resonant sensors based on weakly-coupled resonators. Part 2-Experimental validation

Jérôme Juillard, Ali Mostafa, Pietro Maris Ferreira

Nonlinear operation of resonant sensors based on weakly-coupled resonators: experimental validation

Jérôme Juillard, Ali Mostafa, Pietro Maris Ferreira

Abstract - This paper is aimed at the validation of a theoretical analysis of the properties of nonlinearly-operated weakly-coupled resonators (WCRs) for resonant sensing applications. In particular, we investigate the relationships between the operating point of such devices and different performance indicators, such as parametric sensitivity, sensitivity to drive level and to noise, and bandwidth. To this end, a couple of high-Q MEMS resonators exhibiting nonlinear restoring and damping forces are used. A careful characterization of the resonators and their associated electronics is made, resulting in a very good, quantitative fit between the experimental results and those predicted by theory.

I Introduction

Because of their large parametric sensitivity and their capacity to reject environmental drift, sensor architectures based on actively- and passively-coupled MEMS resonators are a subject of current research interest [1-4]. While the linear theory of operation of such devices is well-known [5-6], there is little theoretical background concerning their nonlinear (large oscillation amplitude) operation. However, some recent studies show there may be a practical interest to operating in such a regime, demonstrating, on a case-by-case basis, improvement in measurement range [7], signal-to-noise ratio [8], or drive voltage fluctuations [9] for example.

In [10], we have presented a comprehensive theoretical framework for modeling WCRs subject to nonlinear restoring forces, as well as nonlinear damping forces. Based on our analysis, some common characteristics of nonlinear WCRs could be established. In particular, we showed that, for two coupled resonators oscillating at the same amplitude A, the following features could be observed:

- above a nonlinearity-dependent threshold amplitude, the parametric sensitivity to relative stiffness mismatch ϵ of the amplitude ratio R and of the phase difference[1] ϕ decrease as $1/A^2$, regardless of which nonlinearity dominates.
- above this threshold amplitude, unless nonlinear damping forces dominate
    - at most one oscillation state is stable, depending on the sign of the Duffing parameter (and on another system parameter: feedback phase is the case of MILOs, coupling stiffness in the case of MOLOs).
    - the sensitivity to intrinsic (e.g. thermomechanical) noise of R decreases as $1/A^3$.
    - the sensitivity to intrinsic noise of ϕ decreases as $1/A$.
- when damping nonlinearity dominates, the sensitivity to intrinsic noise of ϕ decreases as $1/A^3$.

These properties were demonstrated under several assumptions, mainly that the two resonators are nominally identical (i.e. their relative stiffness mismatch ϵ is 0, they have the same Duffing coefficient γ, the same quality factor Q, the same nonlinear damping coefficient α). Furthermore, they are limited to a narrow bandwidth of quasi-static fluctuations, and an equally narrow range of values of ϵ close to $\epsilon = 0$.

In this paper, we aim at illustrating and commenting these properties in the context of an experimental study, far from the ideal framework of [10]. It should be stressed that we do not seek to demonstrate an hypothetical improvement in performance compared to "conventional" frequency-modulated resonant sensors, but merely to validate our theoretical analysis, provide some helpful examples and gain some critical insight.

[1] As an output metric, phase difference is only relevant for MILOs.

To this end, the setup shown in Fig. 2 is used: it implements a MILO architecture with $\theta = 45°$, consisting of two MEMS resonators and discrete electronic components, as studied in [7]. The circuit and the MEMS resonators are described in section II. In particular, the nonlinear characteristics of the resonators are established, and the connection between electrical measurements and theoretical framework is made. Section III is dedicated to an experimental sensitivity analysis of the system, aimed at validating the quasi-static model of [10]: this provides a first, indirect proof of our claims regarding sensitivity to intrinsic noise of WCRs. Section IV, which is focused on the spectral analysis of the measured signals, illustrates the finite bandwidth of these systems. Section V is dedicated to a discussion and some concluding remarks.

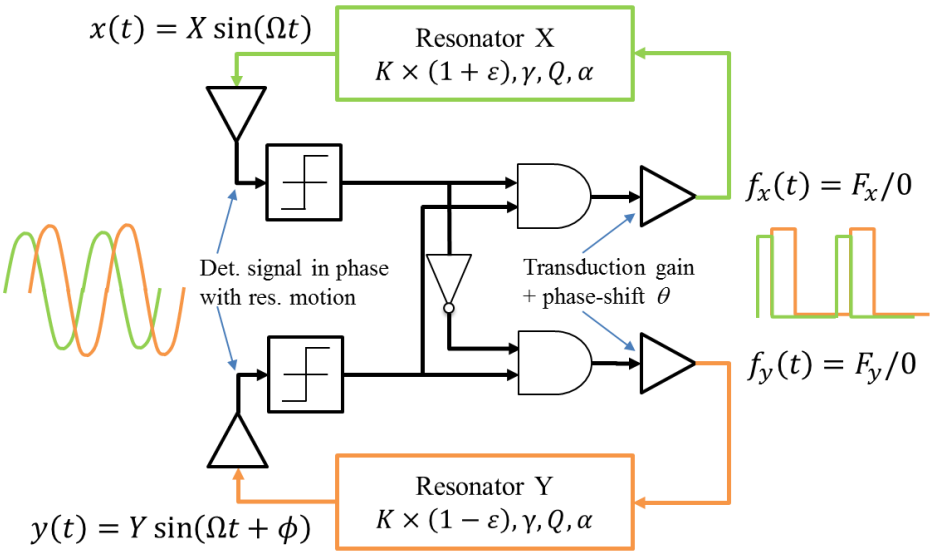

Fig. 1 – System-level view of a MILO based on a digital mixer, as in [10].

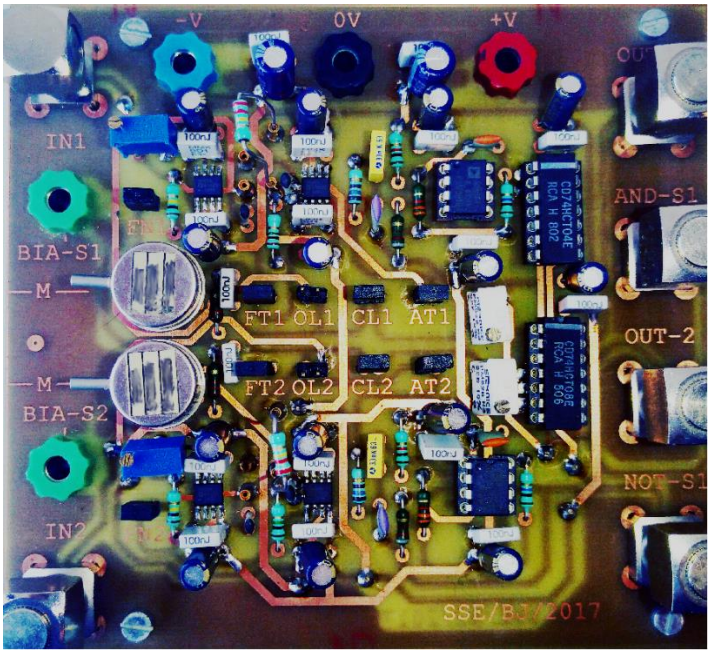

Fig. 2 – PCB implementation of a MILO with discrete components.

II Description of the setup[2]

II-1 MEMS resonators

The MEMS resonators used in these experiments are two vacuum-packaged resonant gauges taken from P90 pressure sensors, presented in [11] and characterized in detail in [12-13]. These one-port resonators consist in an electrostatically-actuated and capacitively-detected silicon beam, with natural frequency $f_0 \approx 69\text{kHz}$ and quality factor $Q \approx 2 \times 10^4$. One end of the beam is perfectly clamped while the other is attached to the membrane used as a pressure sensing element. As a consequence of this imperfect clamping condition, no stress-stiffening is observed in the gauges, even at very large oscillation amplitudes [12], electrostatic softening being the dominant source of nonlinearity as far as nonlinear restoring forces are concerned. As reported in [14], internal resonances also occur in these resonators outside of their nominal operating range, resulting in an apparent decrease of their quality factor. This may adequately be modelled as a nonlinear damping phenomenon, as shown in section II-3.

II-1-a Simplified model of the resonators

Each resonator is accurately described by a single-DOF non-dimensional model resulting from the Galerkin projection of the electrostatically-actuated Euler-Bernoulli beam equation on the first clamped-clamped beam eigenmode [15]:

$$(1+\kappa)x + \left(\frac{1}{Q_x} + \alpha_x x^2\right)\frac{dx}{dt} + \frac{d^2x}{dt^2} = \delta_x \frac{\left(1+v_x(t)\right)^2}{(1-x)^{3/2}}, \qquad \text{(1-a)}$$

$$(1-\kappa)y + \left(\frac{1}{Q_y} + \alpha_y y^2\right)\frac{dy}{dt} + \frac{d^2y}{dt^2} = \delta_y \frac{\left(1+v_y(t)\right)^2}{(1-y)^{3/2}}, \qquad \text{(1-b)}$$

where x or y designates the relative displacement of the center of the beam with respect to the electrostatic gap, κ is a parameter representing the mechanical detuning of the resonators with respect to their average unbiased natural frequency, δ_x (resp. δ_y) is an electromechanical transduction coefficient, proportional to the square of bias voltage V_{bx} (resp. V_{by}), and $v_x \ll 1$ (resp. v_y) is the ratio of the drive voltage V_{drvx} (resp. V_{drvy}) of the resonator to its bias voltage. Expanding the numerator of the right-hand side to 3rd order and dropping the DC terms and the v_x^2 and v_y^2 terms, we obtain:

$$x\left(1+\kappa-\frac{3}{2}\delta_x-\frac{35}{16}\delta_x x^2\right) + \left(\frac{1}{Q_x} + \alpha_x x^2\right)\frac{dx}{dt} + \frac{d^2x}{dt^2} = 2\delta_x\left(1+\frac{15}{8}x^2\right)v_x(t). \qquad \text{(2-a)}$$

$$y\left(1-\kappa-\frac{3}{2}\delta_y-\frac{35}{16}\delta_y y^2\right) + \left(\frac{1}{Q_y} + \alpha_y y^2\right)\frac{dy}{dt} + \frac{d^2y}{dt^2} = 2\delta_y\left(1+\frac{15}{8}y^2\right)v_y(t). \qquad \text{(2-b)}$$

Note that the resulting model is nearly identical to (1) in [10], the main difference being the actuation nonlinearity appearing on the right-hand side, which is known to induce waveform-dependent phenomena [12]. This effect is studied in section II-2.

II-1-b Electrostatic tuning of the resonators

The resonators can be tuned by choosing their bias voltages so that

$$2\kappa - \frac{3}{2}(\delta_x - \delta_y) = 0. \quad (3)$$

Changing the bias voltage of resonator y by a small amount from V_{by} to $V_{by} + \Delta V_{by}$, for instance, simulates a mechanical stiffness mismatch according to:

[2] Note that, in the experiments of sections II, III and IV, no particular precaution is taken to control temperature, ambient pressure or other environmental factors.

$$\epsilon \approx \frac{3}{2}\frac{\Delta V_{by}}{V_{by}}\delta_y. \quad (4)$$

Note that this also induces a change in the Duffing coefficient of the resonator and in the amplitude of its driving force.

Measuring the MILO's oscillation frequency at small oscillation amplitudes for different bias voltages yields the following relation between the electromechanical transduction coefficient and bias voltage

$$\delta_{x,y} \approx \chi \times V_{bx,y}^2 \qquad (5)$$

with $\chi = -3.35 \times 10^{-6}$.

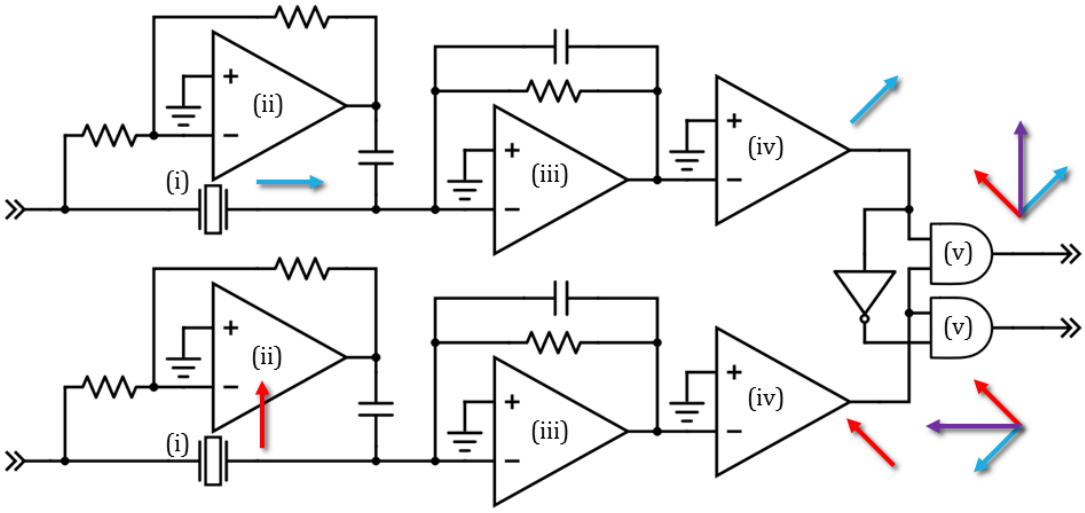

Fig. 3 – Schematic of the studied MILO, consisting of (i) MEMS resonators, (ii) feedthrough compensation stages, (iii) readout stages, (iv) comparators and (v) logic gates. The resistive bridges used for setting drive voltage values have been omitted, and passive bandpass filters at the comparators inputs as well. The arrows near (i) correspond to the phasor representation of the mechanical oscillations when $\epsilon = 0$, those near (iv) to that of the electrical oscillation at the comparator output, highlighting that when $\theta = 45°$, the digital mixer then generates actuation voltages (purple arrows) with a 90° phase-lead with respect to the mechanical motion.

II-2 Electronic circuit and transduction

A schematic of the studied MILO is represented in Fig. 3. We first give a general description of this circuit, before focusing on how motional oscillation amplitudes or actuation forces may be derived from the electrical signals.

II-2-a General description of the oscillator loop

The motional signals are amplified with transimpedance amplifiers, with equal values of the resistive and capacitive part of the feedback impedance at resonance, i.e. $C_f = 15\text{pF}$, $R_f = 160\text{k}\Omega \approx 1/2\pi f_0 C_f$. This results in a 45° phase-lag compared to a regular charge amplifier (with $R_f \gg 1/2\pi f_0 C_f$). The output voltage V_{outx} then satisfies

$$\frac{dV_{outx}}{dt} + V_{outx} = -\frac{V_{bx}}{2}\frac{C_0}{C_f}\frac{dx}{dt} \times \frac{1}{(1-x)^{3/2}}, \quad (6)$$

where $C_0 \approx 0.5\text{pF}$ is the nominal capacitance of the resonator. Note that the capacitance changes as the inverse of the square root of x because of the non-uniform deformation along the length of the beam [15]. Note also that (6) only holds provided capacitive feedthrough is properly cancelled. In our

setup, feedthrough cancellation is enforced via an active attenuator stage in parallel with the resonator, as illustrated in Fig. 3. Low-noise, high-speed AD8065 operational amplifiers are used for these two stages.

The binary-valued drive signals V_{drvx} and V_{drvy} are generated through a set of comparators (AD8561), logic gates (74HCT04 and 74HCT08) and potentiometers, as in [7]. Passive bandpass filters are used at the comparator inputs to attenuate unwanted signals below 6kHz or above 600kHz. A small amount of high-frequency hysteresis is also introduced, as proposed in [16]. All in all, simulations and measurements show that the phase delay introduced by the mixer is nearly independent of the amplitude or the harmonicity of its inputs, so that the electronics enforce the condition $\theta = 45°$ regardless of the oscillation amplitude, provided it is significantly higher than a few mV.

Small and large-amplitude waveforms are shown in Fig. 4, highlighting the efficiency of the feedthrough removal, and also the distortion resulting from the detection nonlinearity for large values of motional oscillation amplitudes X and Y.

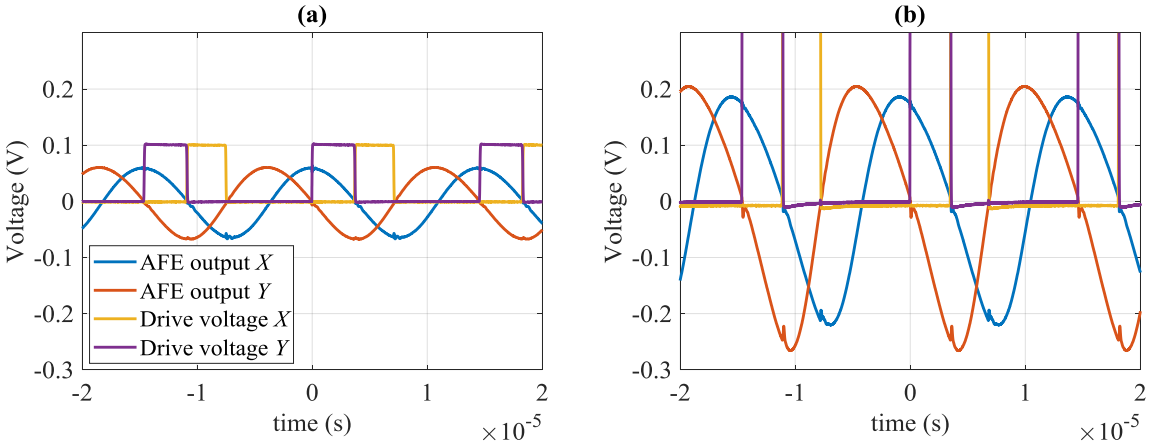

Fig. 4 – Typical waveforms at the AFE outputs and at the resistive bridge outputs when $V_{bx} = 40$V, and $V_{by} \approx 36$V, so that $\phi \approx 90°$, in the cases (a) $V_{drvx} = V_{drvy} = 100$mV, and (b) $V_{drvx} = V_{drvy} = 1$V.

II-2-b Transduction

From (6), one may determine the relation between the RMS value at the amplifier output, which is measured in our experiments, and the mechanical oscillation amplitude. To this end, the solution of (6) is calculated assuming the input $x(t)$ is harmonic, i.e. $x(t) = X \sin \omega t$, and approximating the output V_{outx} with harmonic balance (20 harmonics are used). Then a simple model is fitted to infer X from the RMS value of V_{outx} (Fig. 5, solid line). This relation may be approximated as follows:

$$X = \frac{Z}{1+0.5Z^2}, \qquad \text{(7-a)}$$

$$Z = 4\frac{C_f}{C_0}\frac{\mathrm{RMS}(V_{outx})}{V_{bx}}. \qquad \text{(7-b)}$$

with 0.8% accuracy up to 50% of the gap. In our setup, the ratio C_f/C_0 is measured to be equal to 35.

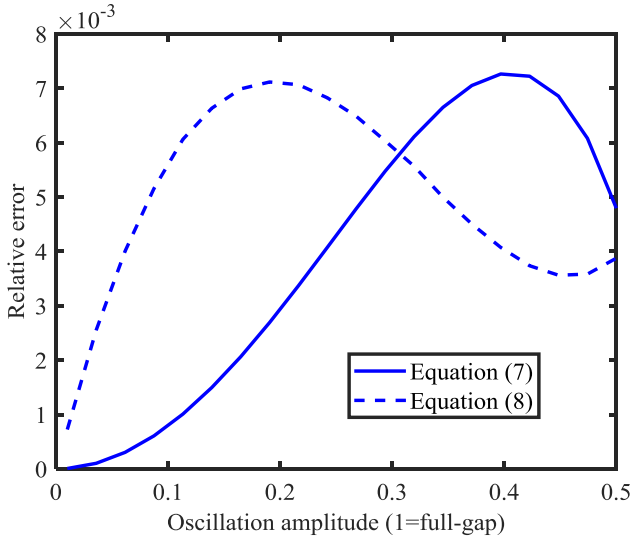

Fig. 5 – Relative error between X as estimated by (7) and actual value (solid line), and relative error between $F_{x,y}$ as estimated by (8) and actual value (dashed line).

With the same approach, one may also determine how the amplitude of the actuation force is related to that of the drive voltage. Two opposing effects result in a nearly perfectly linear relation between these two quantities. First of all, simulations show that, when the resonators oscillate in quadrature, the duty cycle at the comparator output decreases from 25%, when $X = Y \ll 1$, to 23.7% when $X = Y = 0.5$. This phenomenon, which results from the anharmonicity of the AFE outputs, tends to make the drive slightly less efficient at large oscillation amplitudes. However, it is compensated by actuation nonlinearity, whose impact may also be assessed with harmonic balance. Our simulations (Fig. 5, dashed line) show that the following expression may be used for the forces appearing in equation (14) in [10], provided $X = Y = A$,

$$F_{x,y} = 2 \times \delta_{x,y} \times \frac{V_{dx,y}}{V_{bx,y}} \times (1 + \beta A), \qquad (8)$$

where $V_{dx,y}$ is the peak value of $V_{drvx,y}$, and $\beta \approx -0.13$. This expression takes into account the effect of actuation nonlinearity and harmonic distortion of the mixer inputs: the fact that $\beta < 0$ shows that, on the whole, the drive becomes less efficient as X increases. However, neglecting this term leads only to a 6.5% maximum error in the estimation of the driving force at 50% of the gap, so that the following expression is used instead of (8)

$$F_{x,y} = 2 \times \delta_{x,y} \times \frac{V_{dx,y}}{V_{bx,y}}, \quad (9)$$

with little loss in accuracy.

II-3 Characterization of nonlinear damping

The presence of nonlinear damping in the resonators used in the present work was observed, but not fully characterized, in [14]. Here, this phenomenon is evidenced by the fact that, between Fig. 4-a and Fig. 4-b, the oscillation amplitude at the amplifier output increases by a factor which is much less than 10, although the drive voltage goes from 100mV to 1V. One may precisely estimate the quadratic damping coefficients of the resonators through the relation between their oscillation amplitude and their excitation force. Indeed, when the resonators oscillate in quadrature, we have

$$X\left(\frac{1}{Q_x} + \frac{1}{4}\alpha_x X^2\right) = F_x \frac{\sqrt{2}}{\pi}, \qquad Y\left(\frac{1}{Q_y} + \frac{1}{4}\alpha_y Y^2\right) = F_y \frac{\sqrt{2}}{\pi}. \qquad (10)$$

These reduce to (23) in [10] if the damping/driving characteristics of the resonators are identical.

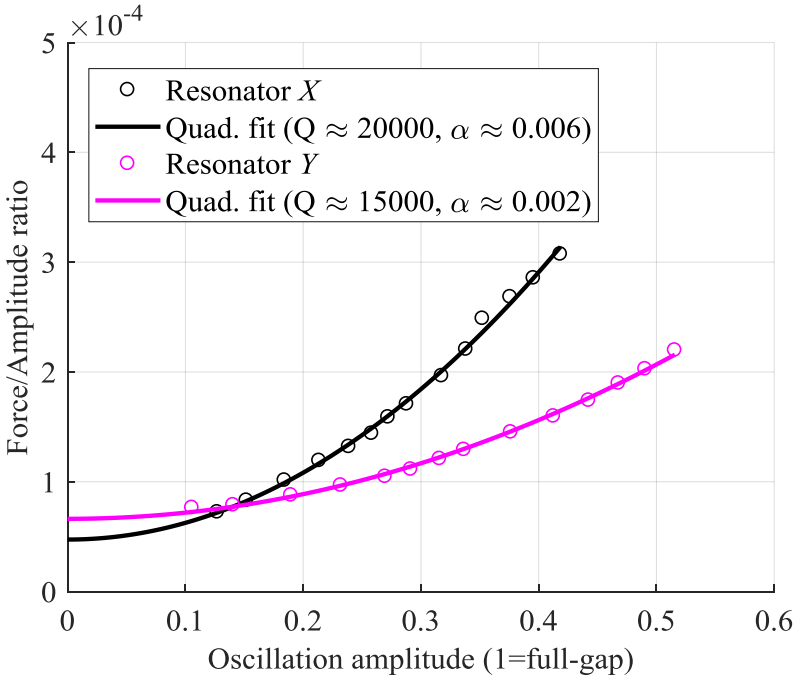

Fig. 6 – Characterization of nonlinear damping. Experimental measurements (circles) and quadratic fits (full lines).

We represent in Fig. 6 the experimental curves of the F_x/X and F_y/Y ratios obtained with $V_{bx} = 40V$ and $V_{by} = 36V$, for drive voltages ranging between 50mV and 1V. For each point, the value of the oscillation amplitude is obtained from the measured RMS voltage through (7), and the value of the force is derived from (9). This figure confirms the quadratic dependence of the damping coefficient to the oscillation amplitude. The (inverse of the) quality factor of each resonator is obtained by extrapolating the quadratic fit of the data to zero oscillation amplitude.

Repeating this experiment for other values of V_{bx} and V_{by} shows that quality factors Q_x and Q_y do not depend on bias voltage, but that coefficients α_x and α_y do. This observation is consistent with the hypothesis that, in our MEMS devices, nonlinear damping results from internal resonance, as considered in [14].

III Experimental sensitivity analysis

III-1 Experimental protocol

We are interested in verifying the consistency of the models established in [10], regarding the sensitivity to mismatch and the sensitivity to intrinsic noise of MILOs in the nonlinear regime. In this sub-section, we explain how these quantities may be experimentally assessed.

III-1-a Sensitivity to mismatch

Sensitivity to mismatch is straightforward to measure. This is done in two steps. First, for a given peak drive voltage $V_{dx} = V_{dy}$, and a given value of V_{bx}, one adjusts V_{by} so that the two resonators oscillate in quadrature ($\phi = 90°$) – practically, this condition is obtained by finding the value of V_{by} for which the duty cycle of V_{drvx} is equal to that of V_{drvy}. The corresponding mechanical oscillation amplitudes (X and Y) and amplitude ratio are estimated from the RMS values of V_{outx} and V_{outy} with (7).

Then, a stiffness variation is induced by changing the value of V_{by} by ΔV_{by} (by an "infinitesimal" amount, about 1% in all of our experiments), with the corresponding change in ϵ given by (4). The resulting phase difference variation $\delta\phi$ and amplitude variations δX and δY are measured.

The sensitivity to mismatch can then be calculated by differentiating the results obtained in the two steps with respect to ϵ. These two steps are repeated for different values of the drive voltage (ranging between 50mV and 1V) and of the bias voltage V_{bx} (from 25V to 40V).

III-1-b Sensitivity to noise

Sensitivity to noise is more tricky to determine. However, this quantity may be assessed by purely deterministic means: considering that thermomechanical noise amounts to four independent force components (n_{cosx}, n_{cosy}, n_{sinx}, n_{siny}) acting on the resonator, one may emulate the effect of a change in one of these components simply by changing the drive level of one of the resonators independently from that of the other. For example, when $\epsilon \approx 0$, changing F_y by an amount δF_y in our MILO modifies equation (15-b) in [10] to

$$\frac{\dot{\delta Y}}{Y_0} = -\frac{1}{2}\left(\frac{1}{Q_y} + \frac{3}{4}\alpha_y Y_0^2\right)\frac{\delta Y}{X_0} + \frac{1}{4}\left(\frac{1}{Q_y} + \frac{1}{4}\alpha_y Y_0^2\right)\delta\phi + \frac{1}{2Y_0}\left(n_{cosy} + \frac{\sqrt{2}}{\pi}\delta F_y\right), \qquad (11)$$

while leaving equations (15-a) and (15-c) unchanged (neither δF_y nor n_{cosy} appear in them). It is then straightforward to show that:

$$\left|\frac{\partial R}{\partial F_y}\right| = \frac{1}{\pi}\left|\frac{\partial R}{\partial n}\right|. \quad (12)$$

Furthermore, for large oscillation amplitudes (with respect to either A_{Duff} or A_{damp}), we also have

$$\left|\frac{\partial \phi}{\partial F_y}\right| = \frac{1}{\pi}\left|\frac{\partial \phi}{\partial n}\right|. \quad (13)$$

Hence, the sensitivity to noise may be determined in a two-step process, as above, but this time the second step consists in changing the value of V_{dy} by a small amount ΔV_{dy} (from 20mV to 50mV, as V_{dy} changes from 100mV to 1V), with the corresponding change in driving force given by

$$\Delta F_y = 2 \times \delta_y \times \frac{\Delta V_{dy}}{V_{by}}. \quad (14)$$

III-1-c Model comparison

All the model parameters are summed up in table 1. Except for C_f/C_0, all the parameters are obtained by characterizing the resonators, as explained in section II: the value of χ is obtained by measuring the electrostatically-induced frequency shift, while damping related parameters are obtained by fitting parabolas to the F_x/X vs. X and F_y/Y vs. Y curves. Note that this last step requires C_f/C_0 to be known. The values of $Q_{x,y}$ and $\alpha_{x,y}$ given in table 1 are those obtained for $C_f/C_0 = 32.5$. This value of 32.5 is within component tolerances of the nominal value (equal to 30) of C_f/C_0, and gives a slightly better fit between the model and the experimental results, as shown in section IV.

Parameter	C_f/C_0	χ	Q	α	α
Unit	no dim.	V^{-2}	no dim.	no dim.	no dim.
Condition				$V_{bx} = 25V$	$V_{bx} = 40V$
Resonator x	32.5	-3.35×10^{-6}	19.5×10^3	11.7×10^{-3}	6.68×10^{-3}
Resonator y			14.4×10^3	1.73×10^{-3}	2.66×10^{-3}

Table 1 – Model parameters used in section IV.

IV-2 Results

Experimental results obtained with the protocol described in the previous section are shown in Fig. 7. The results obtained with a quasi-static model of the fluctuations (continuous lines) are superposed to the experimental data (crosses and circles). In order to improve the readability of this experimental sensitivity analysis, the sensitivities to noise and to mismatch are represented versus the average oscillation amplitude:

$$A_{avg} = \frac{X+Y}{2}. \quad (15)$$

We can verify that there is a very good fit between the model and the experimental data. There is a quantitative fit for most curves over several orders of magnitude, except in the case of sensitivity to mismatch at $V_{bx} = 25V$, where the model systematically overestimates sensitivity by about 3dB. However, even in that case, the experimental and simulated results have highly similar trends. Thereby, the theoretical analysis of [10] is validated.

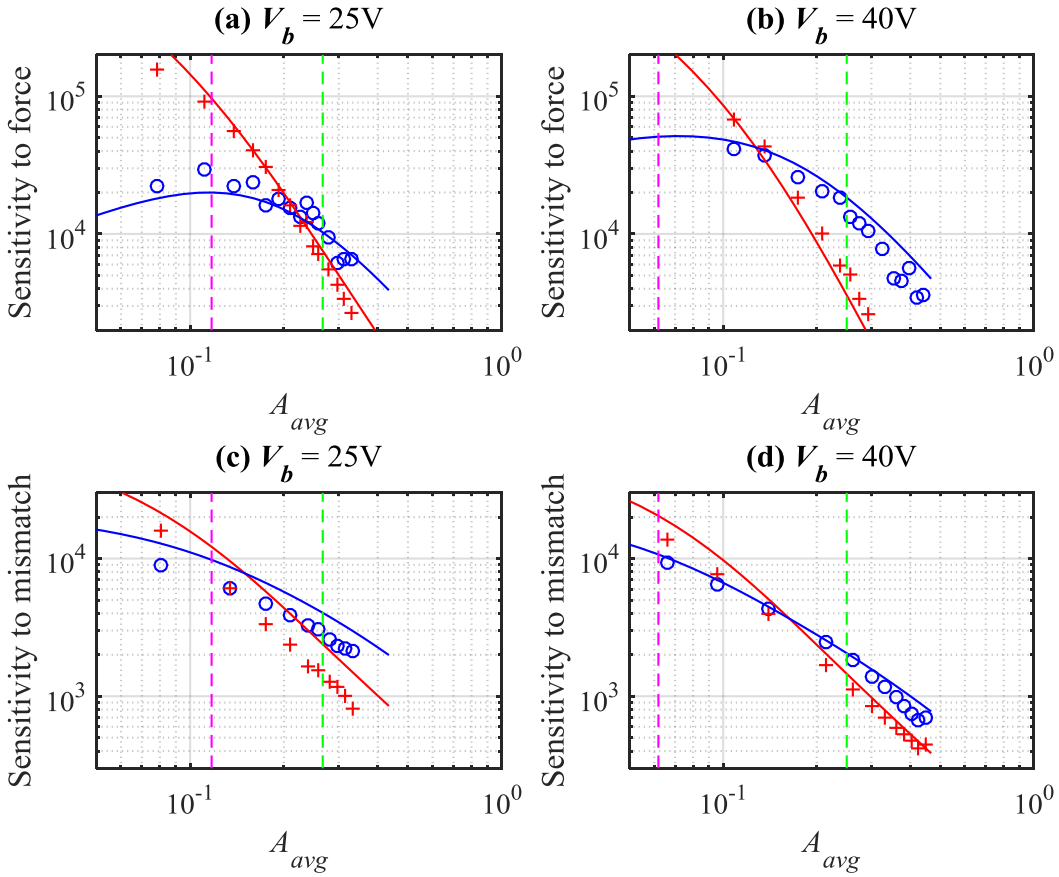

Fig. 7 – Experimental (circles and crosses) and simulated (full lines) sensitivities of the MILO with different operating conditions. Blue corresponds to phase difference, red to amplitude ratio. Vertical dashed lines correspond to the average critical Duffing (magenta) and damping (green) amplitudes of the resonators.

The two sets of results are qualitatively different in the sense that, in the case $V_{bx} = 25V$ (and $V_{by} \approx 17V$), the average critical Duffing amplitude is about twice as large as in the case $V_{bx} = 40V$ (and $V_{by} \approx 36V$) - 11% of the gap, as opposed to 6% of the gap. On the other hand, the critical damping amplitude is relatively unchanged - 28% of the gap in the first case, and 26% in the second. Thus, in the case $V_{bx} = 40V$, there is a wider region in which nonlinear stiffening dominates, in which the sensitivity to force (and hence to intrinsic noise) of the phase-difference decreases at a much

slower rate than its sensitivity to mismatch. In the same region, the sensitivity to force of the amplitude ratio decreases with A_{avg} much faster than that of the phase difference. Since the sensitivities to mismatch of these two quantities decrease at approximately the same rate, the FOMs of the different output metrics (extrapolated from our model) are quite different, depending on whether $V_{bx} = 25\text{V}$ or $V_{bx} = 40\text{V}$, as shown in Fig. 8.

Systematic errors may result from our overlooking the dependence on bias voltage of a system parameter: for example, the static deformation of the resonator beam (and consequently C_f/C_0), which is bias voltage-dependent, is not accounted for. Moreover the expressions of the electrostatic force used in (1) and that of the motional current used in (6) are valid in the case of an initially straight clamped-clamped beam oscillating along its first eigenmode [15], whereas, in the present case, the beam has a pressure-induced initial deformation, which also influences the electrostatic softening coefficient. However, we do not have sufficient data to accurately account for these effects and must content ourselves with the current model. Measurement errors are of a different nature depending on whether the oscillation amplitude is small or large (the amplitude span of our experiment is from 0.05% to 50% of the gap): at small amplitudes, the sensitivity to mismatch is large (on the order of 14×10^3), making it difficult to manually tune V_{by} to obtain $\phi = 90°$. Furthermore, the sensitivity to driving force fluctuations (and more generally to noise) is also large, which results in unstable readings. At large amplitudes, both sensitivities are considerably reduced (by about one order of magnitude, concerning the sensitivity to mismatch), and are therefore more difficult to estimate because of the limited accuracy of the oscilloscope (MSO5204) used in these experiments.

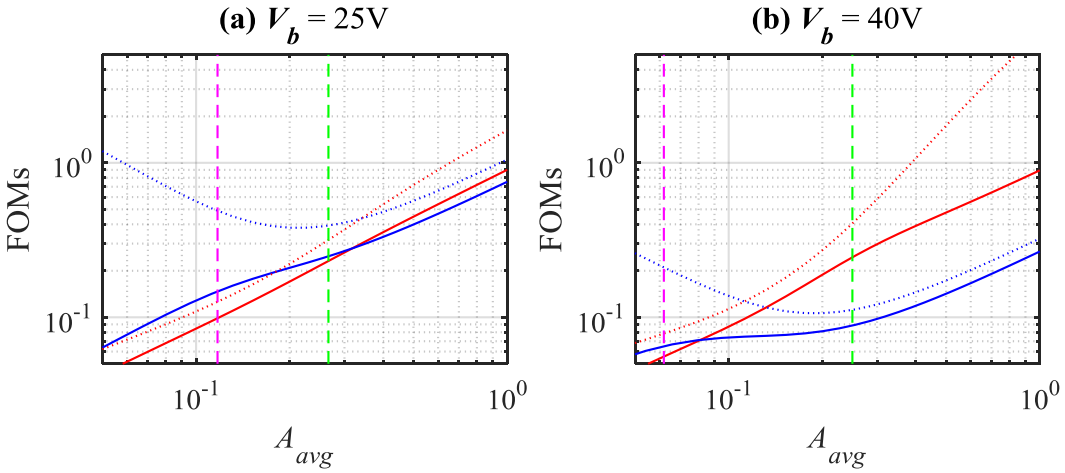

Fig. 8 – Extrapolated FOM of amplitude ratio (red) and of phase difference (blue), for $V_{bx} = 25\text{V}$ (a) and $V_{bx} = 40\text{V}$ (b) vs. oscillation amplitude. Vertical dashed lines correspond to the average critical Duffing (magenta) and damping (green) amplitudes of the resonators. The dotted lines represent the ratio of sensitivity to mismatch over sensitivity to force.

IV Spectral analysis

In this section, we seek to validate the results established in [10] regarding the dynamic behavior of WCRs, through an analysis of the spectra of different output metrics.

IV-1 Experimental protocol

The spectra presented in this section are obtained by setting $V_{bx} = 40V$, and $V_{by} \approx 36V$ so that the resonators oscillate in quadrature. Then 50 consecutive 4-second-long acquisitions of V_{outx} and V_{outy} are taken with a high-resolution 2-channel digitizer (Alazar ATS660, 16-bit digitizer) at a sampling frequency of 500kHz. For each acquisition, V_{outx}^2, V_{outy}^2 and $V_{outx} \times V_{outy}$ are averaged with a sliding

window, yielding an estimate of the fluctuations of R and ϕ over time. Reduced-variance spectra are then obtained by averaging the 50 periodograms resulting from each acquisition (Bartlett's method).

IV-2 Results

The power spectra of the fluctuations of R and ϕ obtained at three oscillation amplitudes (A_{avg} varying from 0.26 to 0.46) are represented in Fig. 9-a and Fig. 9-b. The measured noise levels are much larger than the thermomechanical noise floor or than our digitizer's. They are consistent with the voltage fluctuations of the power supplies (of about 3mV peak-to-peak), which result, through V_{bx} and V_{by}, in additive measurement noise at the AFE's output, and in variations of ϵ around 0. More precisely, assuming $V_{bx}(t) = \overline{V_{bx}} + v_{bx}(t)$, equation (6) becomes:

$$\frac{dV_{outx}}{dt} + V_{outx} \approx -\frac{\overline{V_{bx}}}{2}\frac{C_0}{C_f}\frac{dx}{dt} \times \frac{1}{(1-x)^{\frac{3}{2}}} - \frac{C_0}{C_f}\frac{dv_{bx}}{dt}, \qquad (16)$$

and (4-5) yield:

$$\epsilon(t) \approx -\frac{3}{2}\chi\overline{V_{bx}}v_{bx}(t). \quad (17)$$

The superposition of these two effects can partly explain the measured spectra: measurement noise results in a white noise floor, while the STF of the output metrics – equations (36-38) in [10] – amplifies the variations of ϵ around 0. The simulated spectra accounting only for these two effects are plotted in Fig. 9-c.

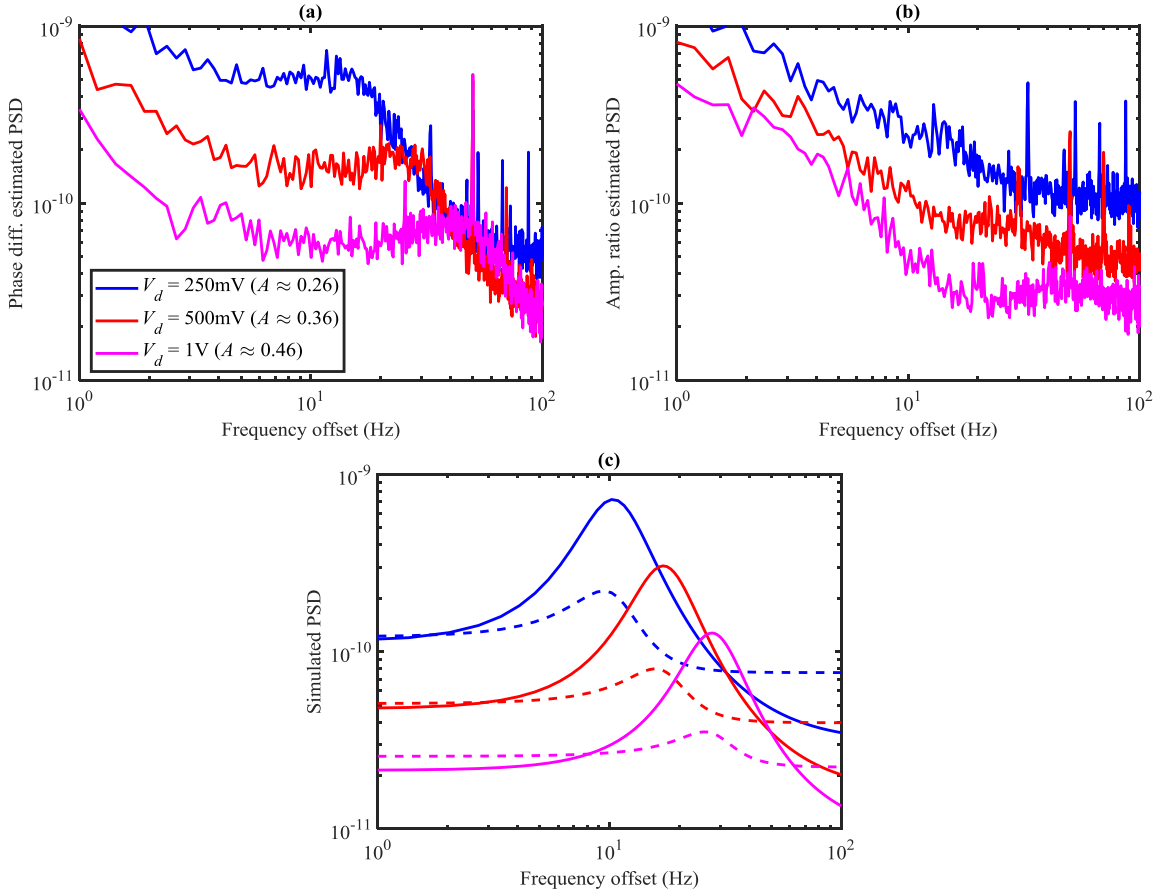

Fig. 9 – Experimental phase difference (a) and amplitude ratio (b) spectra, at three different drive amplitudes. Simulated spectra (c) of phase difference (full lines) and amplitude ratio (dashed lines) assuming fluctuations result only from white bias voltage noise.

We find a rather good agreement between the experimental and simulated spectra of R. The level of the fluctuations at $\Delta\omega_{STF}$ corresponds quite well to what is theoretically predicted (Fig. 9-c), with the characteristic bump in the STF. At very low frequency offset, the experimental spectrum of R is dominated by flicker noise, whose origin is yet unclear. It may well be caused by the active electronics of our circuits, in spite of the precautions that were taken to avoid this phenomenon, or might result from other effects, such as intrinsic mechanical stiffness fluctuations [17].

The comparison of the experimental and simulated spectra of ϕ is more puzzling: although these spectra share some quantitative similarities, the resonance peak in the experimental STF is much less marked than expected. This might be a consequence of the flicker noise which becomes visibly predominant at low frequency offsets. Another explanation may be that the fluctuations of $\Delta\omega_{STF}$ over the time required for doing the 50 measurements cannot be considered infinitesimal (as implicit in the perturbation analysis conducted in [10]), resulting in a spread-out peak in the spectrum of ϕ.

V Conclusion

This paper provides, for the first time, an experimental proof of several results postulated in [10] for nonlinear WCRs with a critical Duffing amplitude smaller than the critical damping amplitude ($A_{Duff} < A_{damp}$). Using two matched resonators displaying such nonlinear behavior, we have verified:

- the similar decrease in parametric sensitivity of R and ϕ in WCRs operated above A_{Duff}.
- the improved robustness to drive-level fluctuations (and hence to intrinsic oscillator noise) of R between A_{Duff} and A_{damp}.
- the amplitude-dependence of the bandwidth in which R and ϕ are sensitive to intrinsic noise and to stiffness mismatch ϵ.

These experimental results were found to be in quantitative agreement with our simulations, which validates the analysis in [10].

As mentioned in section I, sensor performance was not our primary concern. Still, the results presented in this paper may be analyzed in this respect. We have shown that, in the current setup, operating at a large oscillation amplitude results in a wider bandwidth for both R and ϕ, but in no clear gain in terms of input-referred noise (since our noise floor results largely from stiffness mismatch noise). Furthermore, because of the predominance of bias voltage noise over thermomechanical noise, there is little to be gained – in the present case – in using one output metric rather than the other. However, this is not a definitive result, as there remains much room for decreasing electronic noise in our circuit, nor is it a general result.

Finally, several questions remain unanswered, and require further investigation. First, the spread-out outlook of the peaks in the observed experimental spectra is unexplained, although some hypotheses were formulated as to this phenomenon. One may then refine the models in [10] to account for flicker, drift and finite fluctuations of the system parameters, for example by using a non-perturbed model such as (7) in [10] or multiple-scale analysis [18]. More practically, one may also try to reproduce the experiments in a carefully controlled environment, or with better-matched resonators (which would more efficiently reject common-mode variations).

Another point that requires further study is the behavior of WCRs when damping nonlinearity dominates: first, as mentioned in [10], there does not seem to be a definitive theory linking thermomechanical noise to nonlinear damping. Decreasing (bias voltage) noise in our setup may then help us investigate this phenomenon. Alternatively, other resonators with increased damping, in particular MEMS resonators operated in ambient atmospheric pressure and subject to squeezed-film damping, may be better suited to this investigation.

References

[1] C. Zhao et al., “A review on coupled MEMS resonators for sensing applications utilizing mode localization”, Sensors and Actuators A, vol. 249, pp. 93-111, 2016.

[2] M. Pandit, C. Zhao, G. Sobreviela, A. A Seshia, “Immunity to Temperature Fluctuations in Weakly Coupled MEMS Resonators”, 2018 IEEE Sensors Conference, pp. 1-4, 2018.

[3] J. Juillard, P. Prache, N. Barniol, “Analysis of mutually injection-locked oscillators for differential resonant sensing”, IEEE Transactions on Circuits and Systems 1, vol. 63, pp. 1055-1066, 2016.

[4] P. Prache, J. Juillard, P. Maris Ferreira, N. Barniol, M. Riverola, “Design and characterization of a monolithic CMOS-MEMS mutually injection-locked oscillator for differential resonant sensing”, Sensors and Actuators A, vol. 269, pp. 160-170, 2018.

[5] P. Thiruvenkatanathan, J. Yan, J. Woodhouse, A. A. Seshia, “Enhancing parametric sensitivity in electrically coupled MEMS resonators”, IEEE Journal of Microelectromechanical Systems, vol. 18, pp. 1077-1086, 2009.

[6] J. Juillard ; P. Prache, P. M. Ferreira, N. Barniol, “Ultimate Limits of Differential Resonant MEMS Sensors Based on Two Coupled Linear Resonators”, IEEE Transactions on Ultrasonics, Ferroelectrics, and Frequency Control, vol. 65, pp. 2440-2448, 2018.

[7] J. Juillard, A. Mostafa, P. M. Ferreira, “Nonlinear enhancement of locking range of mutually injection-locked oscillators for resonant sensing applications”, European Frequency and Time Forum, pp. 109-113, 2018.

[8] J. Juillard, A. Mostafa, P. M. Ferreira, “Analysis of resonant sensors based on mutually injection-locked oscillators beyond the critical Duffing amplitude”, European Frequency and Time Forum, pp. 114-118, 2018.

[9] M. Pandit et al., “Reduction of Amplitude Ratio Dependence on Drive Level in Mode Localized Resonant MEMS Sensors”, IEEE Sensors conference, 3 pp., 2017.

[10] J. Juillard, A. Mostafa, P. M. Ferreira, “Nonlinear operation of resonant sensors based on weakly-coupled resonators: theory and modeling”, available as preprint on HAL, 2019.

[11] J. Mandle, O. Lefort, A. Migeon, “A new micromachined silicon high accuracy pressure sensor”, Sensors and Actuators A, vol. 46-47, pp.129-132, 1995.

[12] A. Brenes, J. Juillard, L. Bourgois, F. Vinci dos Santos, “Influence of the Driving Waveform on the Open-Loop Frequency Response of MEMS Resonators With Nonlinear Actuation Schemes”, IEEE/ASME Journal of Microelectromechanical Systems, vol. 25, pp. 812-820, 2015.

[13] A. Brenes, “Modélisation des phénomènes non-linéaires dans un capteur MEMS résonant pour l'optimisation de ses performances et de sa fiabilité,” Ph.D. thesis, Université Paris-Saclay, 2015.

[14] A. Brenes, J. Juillard, F. Vinci dos Santos, “Electrostatically-induced modal crosstalk phenomena in resonant MEMS sensors”, Symposium on Design, Test, Integration and Packaging of MEMS MOEMS, pp. 1-4, 2014.

[15] J. Juillard, “Analysis of resonant pull-in of microelectromechanical oscillators”, Journal of Sound and Vibration, vol. 350, pp. 123-139, 2015.

[16] AD8561 Datasheet, rev. D, https://www.analog.com/media/en/technical-documentation/data-sheets/AD8561.pdf

[17] M. Sansa et al., “Frequency fluctuations in silicon nanoresonators”, Nature Nanotechnology, vol. 11, pp. 552-558, 2016.

[18] A. H. Nayfeh, D. T. Mook, “Nonlinear Oscillations”, Wiley, 1979.